AGU PUBLICATIONS

JGR

Journal of Geophysical Research: Solid Earth

RESEARCH ARTICLE
10.1002/2013JB010335

Key Points:
- Modeling fault damage zones using dynamic rupture propagation
- Predicting fault damage zone attributes
- Comparison of modeled damage zones with those observed in outcrop

Correspondence to:
M. Johri,
madhurjohri@gmail.com

Citation:
Johri, M., E. M. Dunham, M. D. Zoback, and Z. Fang (2014), Predicting fault damage zones by modeling dynamic rupture propagation and comparison with field observations, *J. Geophys. Res. Solid Earth*, *119*, doi:10.1002/2013JB010335.

Received 5 MAY 2013
Accepted 16 JAN 2014
Accepted article online 20 JAN 2014

Predicting fault damage zones by modeling dynamic rupture propagation and comparison with field observations

Madhur Johri[1,3], Eric M. Dunham[2], Mark D. Zoback[1], and Zijun Fang[4]

[1]Department of Geophysics, Stanford University, Stanford, California, USA, [2]Now at Upstream Technology, BP America, Houston, Texas, USA, [3]Department of Geophysics and Institute of Computational and Mathematical Engineering, Stanford University, Houston, California, USA, [4]ConocoPhillips Technology and Projects, Houston, Texas, USA

Abstract We use a two-dimensional plane strain dynamic rupture model with strongly rate-weakening friction and off-fault Drucker-Prager plasticity to model damage zones associated with buried second-order thrust faults observed in the SSC reservoir. The modeling of ruptures propagating as self-sustaining pulses is performed in the framework of continuum plasticity where the plasticity formulation includes both deviatoric and volumetric plastic strains. The material deforming inelastically due to stress perturbations generated by the propagating rupture is assumed to be the damage zone associated with the fault. Dilatant plastic strains are converted into a fracture population by assuming that the dilatant plastic strain is manifested in the form of fractures. The cumulative effect of multiple slip events is considered by superposition of the plastic strain field obtained from individual slip events. The relative number of various magnitude slip events is chosen so as to honor the Gutenberg-Richter law. Results show that the decay of fracture density (F) with distance (r) from the fault can be described by a power law $F = F_0 r^{-n}$. The fault constant F_0 represents the fracture density at unit distance from the fault. The decay rate (n) in fracture density is approximately 0.85 close to the fault and increases to ~1.4 at larger distances (>10 m). Modeled damage zones are approximately 60–100 m wide. These attributes are similar to those observed in the SSC reservoir using wellbore image logs and those reported in outcrop studies. Considering fault roughness affects local damage zone characteristics, these characteristics are similar to those modeled around planar faults at a scale (~10 m) that affects bulk fluid-flow properties.

1. Introduction and Motivation

Damage zones are regions of anomalously high fault and fracture density surrounding larger-scale faults. Fractures in damage zones present both problems and opportunities during production from hydrocarbon reservoirs, especially those that have low matrix permeability. The heterogeneity and complexity of fluid-flow paths in fractured reservoirs makes it difficult to predict their behavior. A few field studies have documented the influence of damage zones on production. For example, *Paul et al*. [2009] report a study from the CS gas field (in the Timor gap between Australia and Indonesia) where it is only possible to explain large gas production rates by introducing spatially variable permeability anisotropy (in flow simulators) representative of damage zones present in the reservoir. *Hennings et al*. [2012] report a case from the Suban gas field in SE Asia where the production from wells that sample damage zones is several times greater than those which do not traverse through damage zones.

Since damage zones strongly influence fluid flow in fractured reservoirs, it is important to have sufficient data to characterize and incorporate them in fluid-flow simulators to model flow accurately. Direct observations of fractures and faults at depth in reservoirs typically come from 3-D seismic reflection data, image logs in wellbores, and studies of exhumed core. Of course, 3-D seismic data identify only larger-scale faults and fail to resolve smaller fractures that can strongly influence fluid flow. As core is rarely available over significant ranges of depth, wellbore image data are the best available source of subsurface fracture information. However, these data are one-dimensional and sample only limited parts of a reservoir. Thus, it is difficult to build geologically representative models of reservoirs having damage zones. Our goal is to help develop a methodology for modeling and predicting damage zones associated with reservoir-scale faults (whose position is constrained from seismic images); the damage zone modeling results can be used in conjunction with information on major fracture sets (fracture intensity and orientation) derived from borehole image logs

to build geologically consistent and seismologically constrained fracture networks to inform fluid-flow modeling through fractured reservoirs.

Fault damage zones may be created by various cumulative processes during or after fault formation, including Andersonian fracturing [*Anderson*, 1942; *Scholz*, 2002], early fault tip migration, fault tip linkage, cumulative fault wear with increasing displacement, (which are all quasi-static processes), and damage caused by dynamic rupture events [*Rudnicki*, 1980; *Wilson et al*., 2003; *Paul et al*., 2009]. These models are discussed by *Mitchell and Faulkner* [2009]. In most applications to oil and gas reservoirs, damage zones are modeled as a result of slip on fault planes using static dislocations in elastic media [*Shipton and Cowie*, 2003]. Such models only consider static stress changes. Time dependence of slip is not included. In these models, stress concentrations are limited to fault tips and geometrical irregularities. Regions over which the stresses exceed the rock yield stress are considered to comprise the damage zone of the fault. Since stress concentrations occur only near the ends of fault segments or with other structural discontinuities such sharp bends or offsets in the fault surface, these static dislocation models do not produce damage all along the length of the fault, in contrast to what is observed in outcrop studies. Damage all along the fault length, however, can be replicated by considering multiple slip events along various patches of the fault plane and summing up the damage due to quasi-static dislocation of each slipping fault patch. Nevertheless, the quasi-static models neglect inertial effects, which may be significant.

Dynamic rupture models are fundamentally different from static models. These models consider stress perturbations around the fault tip at each stage of propagation and hence can account for damage all along the length of the rupture [*Madariaga*, 1976; *Kostrov*, 1964; *Andrews*, 1976a]. These models also account for dynamic and inertial effects, which are neglected in the static models. Previously, *Paul et al*. [2009] used principles of dynamic rupture propagation to model damage zones associated with reservoir-scale faults. They used Freund's asymptotic solution of stress perturbations around a propagating rupture tip [*Freund*, 1979] coupled with Kostrov's solution for a circular crack [*Kostrov*, 1964] to calculate stresses induced by slip in regions close to a propagating rupture tip. The induced stresses were then used to calculate the extent of the damage zone by identifying the region around the fault where the induced stress exceeded the rock strength. A shortcoming of this methodology is that the solution of stress concentrations around a propagating crack tip implies a $1/\sqrt{r}$ stress singularity at the tip and exceptionally high stresses very close to the tip. This singularity is a consequence of an instantaneous stress drop on the fault surface leading to an elliptical distribution of displacement on the fault which produces infinite strains at fault tips. The issue of stress singularity can be resolved by tapering the slip toward the fault tips which can be obtained by transitioning the fault strength over a displacement known as the weakening distance. This forms the basis for the slip-weakening model [*Ida*, 1972; *Andrews*, 1976b; *Rice et al*., 2005]. Another shortcoming of the methodology adopted in *Paul and Zoback* [2007] is that the modeling is limited to an elastic domain. Stresses produced around a propagating fault tip in an elastic model are unreasonably large, which is clearly not possible since the material starts deforming inelastically once the stresses exceed the yield stress. This inelastic deformation leads to stress relaxation and limits stresses to reasonable values.

2. Current Study

In this study, we use principles of dynamic rupture propagation to numerically model damage zones formed as a result of off-fault damage created due to slip on a fault surface. As the rupture propagates, stress perturbations are induced around the rupture tip, leading to failure. Rupture propagation is studied using two-dimensional plane strain models. The off-fault material is described by a Drucker-Prager elastic-plastic rheology which is a simple choice for describing granular and cracked materials. A similar assumption has also been made in other published studies on dynamic rupture propagation [*Andrews*, 2005; *Ben-Zion and Shi*, 2005; *Duan and Day*, 2008; *Ma*, 2009; *Templeton and Rice*, 2008; *Viesca et al*., 2008]. The Drucker-Prager yield criterion [*Drucker and Prager*, 1952] is a pressure-dependent modification of the Huber-von Mises yield criterion and is given by

$$\bar{\tau} + \mu(\sigma_{kk}/3) = b \tag{1}$$

where $\bar{\tau}$ is the second invariant of the deviatoric stress tensor, $\sigma_{kk}/3$ is the mean stress, and μ is the Drucker-Prager (DP) friction coefficient while b is the DP cohesion or shear strength at zero mean stress.

The pressure-dependent elastic-plastic formulation described by *Rudnicki and Rice* [1975] reduces to it when μ is assumed to be independent of the stress level. The yield surface defining the shear strength, therefore, is a function of the mean normal stress. In plane strain models, the DP criterion approximates the Mohr Coulomb (MC) criterion which is given by

$$\tau + (\tan\phi)\sigma_n = c \tag{2}$$

where τ and σ_n are shear and normal traction acting on the fault plane, ϕ is the coefficient of internal friction and c is the cohesion. For a two-dimensional stress state where the out-of-plane principal stress is approximated as $\sigma_{zz} = (\sigma_{xx} + \sigma_{yy})/2$, the DP and MC criteria exactly coincide. In such cases, the DP cohesion and friction coefficient are related to the MC coefficients as $b = c\cos\phi$ and $\mu = \sin\phi$. Both the MC and DP criteria idealize the behavior of brittle materials to compressive stresses, but neither fully describes the inelastic behavior of rocks [*Davis and Selvadurai*, 2002; *Colmenares and Zoback*, 2002]. We use the DP criterion since it is easier to implement numerically due to a smooth yield surface. We neglect cohesion since the deformation processes prior to and during fault formation would have intrinsically damaged the surrounding rock leading to near-negligible cohesion values. The coefficient of friction obeys a rate-and-state law that features the direct effect and evolution toward a strongly velocity-weakening steady state friction coefficient. The amount of slip required for the friction to evolve completely (completely weaken) is L. This weakening occurs over a spatial distance of R_0 at the rupture tip. A complete description of the friction law and plasticity formulation is provided in *Dunham et al*. [2011a]. The model parameters chosen to describe the friction law and the off-fault material rheology are given in Appendix A1.

Most dynamic models that simulate rupture propagation with rate-weakening friction have been limited to ruptures in an elastic domain. As a result, extremely high stresses and slip velocities are predicted near the rupture front. *Noda et al*. [2009] predict maximum slip velocity exceeding 100 m/s and strains of order 0.1. These stresses are far greater than yield stresses, which is inconsistent. Once the yield stress is exceeded, the region around the fault deforms inelastically, leading to stress relaxation, dissipation of energy, and formation of the associated damage zone. Accounting for plasticity prevents unreasonably large stresses and limits the slip velocities to ~10 m/s [*Dunham et al*., 2011a], consistent with the estimates of *Sleep* [2010].

Experimental evidence suggests that frictional resistance decreases very significantly (up to 1 order of magnitude) at coseismic slip rates (~1 m/s) during earthquakes [*Tsutsumi and Shimamoto*, 1997; *Tullis and Goldsby*, 2003a, 2003b; *Prakash and Yuan*, 2004; *Hirose and Shimamoto*, 2005; *Beeler et al*., 2008; *Di Toro et al*., 2011; *Goldsby and Tullis*, 2011]. This is known as dynamic weakening. A consequence of dynamic weakening is that for a certain range of initial stress conditions, ruptures propagate as self-healing slip pulses instead of as cracks [*Cochard and Madariaga*, 1994; *Zheng and Rice*, 1998; *Noda et al*., 2009; *Dunham et al*., 2011a]. The understressing theory developed by *Zheng and Rice* [1998] shows that for ruptures in elastic solids, a critical background shear stress level (τ^{pulse}) exists below which ruptures cannot propagate as cracks. The mode of rupture propagation is uncertain above this critical stress level, but numerical simulations suggest that there is a narrow range of background stress levels around the critical stress level at which ruptures propagate as self-sustaining slip pulses [*Cochard and Madariaga*, 1994; *Zheng and Rice*, 1998; *Noda et al*., 2009]. This phenomenon is also observed for shear ruptures in laboratory experiments [*Lykotrafitis et al*., 2006]. Substantial evidence supports the idea that ruptures propagate as self-sustaining slip pulses instead of cracks. The duration of slip at a point on a fault calculated from seismic inversions is much shorter than expected from crack-like propagation models [*Heaton*, 1990]. Simulation results show that only pulse-like propagation honors the scaling between slip and rupture length and that the slip for crack-like propagation is an order larger [*Noda et al*., 2009]. It is expected that natural faults are most likely to host ruptures soon after the stresses build up to the minimum level that would support pulse-like propagation provided nucleation events are sufficiently frequent. Although crack-like propagation is certainly possible at higher stress levels, the likelihood decreases as stresses keep building. Potentially, it may be possible to quantify the probability of the propagation mode as a function of background shear stress levels under given constraints on the rate of nucleation events from sources such as background seismicity,

or earthquake cycle simulations that produce a realistic distribution of event sizes. In this study, we assume that ruptures propagate as self-sustaining pulses.

We use this approach to model damage zones formed due to slip on reservoir-scale second-order, buried, thrust faults observed in the SSC reservoir. Since the modeling is performed in a continuum framework, results obtained are in terms of plastic strains. In order to facilitate comparisons with field observations of fracture density (number of fractures per unit length), plastic strains are converted into a fracture population by assuming the volume created by plastic strains to be expressed in the form of fractures and considering appropriate fracture dimensions. Since the observed damage zones are a result of several slip events of various magnitudes that the fault may have hosted, we account for them in the modeling workflow by superposing the plastic strain field due to several slip events of various sizes, such that the magnitude of those slip events and their frequency are consistent with the Gutenberg-Richter scaling law. We then compare the modeled damage zones with field observations. A discussion of observations and characterization of damage zones at depth that includes field observations from the SSC reservoir is provided in M. Johri et al. (A scaling law to characterize fault damage zones at reservoir depths, submitted to the *American Association of Petroleum Geologists*, 2012). They report 50–80 m wide damage zones in which the decay of fracture intensity with distance from the fault can be described by a power law, the rate of decay between 0.4 and 1.

Information derived from modeling can then be used to constrain the magnitude and extent of damage in the material off of the fault. This information, used in conjunction with knowledge of fracture density and orientations (from borehole image data), can facilitate us in building more geologically constrained and seismologically consistent fracture network models which, in turn, can help constrain fluid-flow modeling through damage zones and fractured reservoirs.

3. Area of Study: SSC Reservoir

We model damage zones associated with second-order thrust faults (~3 km long) in the SSC reservoir (actual name and location withheld due to proprietary reasons). This field produces hydrocarbons from compressionally uplifted, fractured, crystalline and metamorphic basement, and overlying sedimentary rocks. Active deformation has partitioned the reservoir into distinct structural and stress domains. Figure 1 presents a perspective view of the field showing the master fault and 27 second-order faults identified in seismic images. The map lengths of the second-order faults vary from 50 m to 3 km. All seismically resolvable faults have reverse slip. They strike subparallel to the master fault and are concentrated in a 1×8 km area along the crest of the anticline. The fault dips lie between 55° and 80°. The maximum throw across these faults ranges from 8 to 180 m. There is uncertainty regarding the downdip extent and trajectory of most faults due to poor seismic reflectivity at depth; therefore, a conservative approach is adopted and only the fault surfaces with direct seismic evidence are interpreted.

Five wells have been studied in this area—wells A, B, C, E, and I (their locations have not been shown in Figure 1 due to proprietary reasons). Wells A, E, and I are near vertical wells, while wells B and C are deviated wells. Well tests indicate that there is poor correlation between wellbore-reservoir contact length and wellbore performance. In fact there is also a very weak correlation between well performance and the total number of fractures that they intersect. However, there is a strong correlation between the total number of critically stressed fractures transected by the wellbore and well performance. Wells B and C were drilled with the intention of maximizing the borehole intersection with reservoir-scale second-order faults and their respective damage zones containing a rich population of critically stressed faults. As expected, wells B and C were extremely productive, with potential production rates 3 to 7 times higher than previously drilled wells. With the critical role of damage zones in influencing flow and production clearly evident, we aim to model these damage zones associated with second-order faults so that we can eventually incorporate them in flow simulation models.

In order to determine whether the second-order faults slipped in the present-day stress state or in the geologic past under a different stress state, we study the present-day stress regime, orientation of second-order faults, and the nature of faulting. The present-day strike-slip stress field and the steeply dipping fault orientations cannot explain the reverse slip across faults observed in 3-D seismic images. Therefore, we conclude that these second-order faults must have slipped in the geologic past under a reverse faulting stress

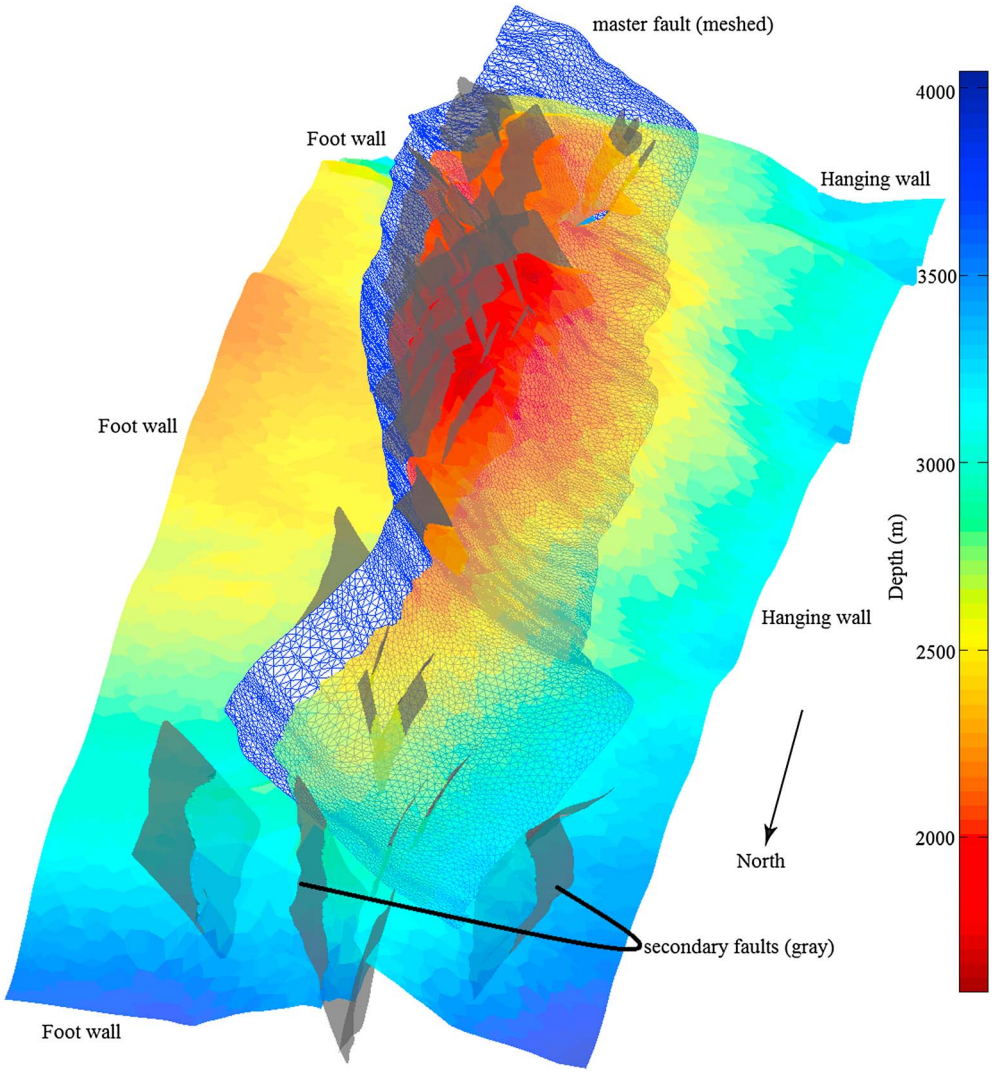

Figure 1. Three-dimensional structural model of the southwestern domain, viewed from the north. The model shows the master fault (first-order fault) and second-order faults. The colored surface represents the depths of the upper horizon of the reservoir.

regime and a rotated configuration (so that the faults have shallow dipping angles (~30°)) that promotes thrust faulting. Stratigraphic studies suggest that changes in the depth of faults from the free surface may not be significant, so we are not required to depth shift the faults for modeling purposes.

4. Model Development and Initial Conditions

1. *Model setup*: We consider a reverse fault dipping 30° in a homogeneous half space representing an optimally oriented fault (Figure 2). The fault is 3 km long. Since there is uncertainty regarding the downward extent of these faults due to poor seismic image quality, we assume the dip length of the fault to be equal to the strike length which is easier to identify in seismic images. The top of the model represents the free surface. The fault does not break the surface. An absorbing boundary condition is applied to the bottom and sides of the blocks, and a traction free boundary condition is applied to the surface. We place the origin at the center of the fault located at 2.2 km depth. Ruptures may propagate bilaterally or unilaterally along the fault surface. In this paper, we will show an example of a rupture that nucleates at the center of the fault (origin) and propagates bilaterally in both directions, and another example of a rupture that nucleates close to the lower extent of the fault and propagates unilaterally along the updip direction.

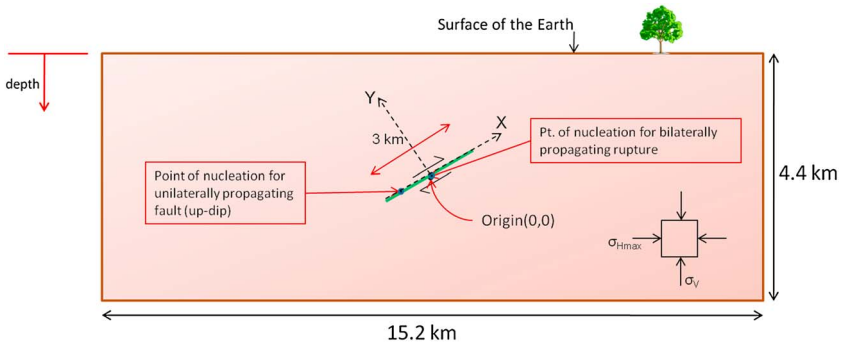

Figure 2. Two-dimensional idealization to model slip on a buried thrust fault dipping at 30°. The green line represents the fault surface. *X* axis is aligned along the fault in the updip direction.

2. *Fault profile*: We have considered both planar and nonplanar faults. Previous studies suggest that natural fault surfaces exhibit deviations from planarity at all scales [*Brown and Scholz*, 1985; *Power et al*., 1988; *Power and Tullis*, 1991, 1995; *Lee and Bruhn*, 1996; *Renard et al*., 2006; *Sagy et al*., 2007; *Candela et al*., 2009; *Candela and Renard*, 2012]. Observations demonstrate that faults are self-similar fractal surfaces [*Power and Tullis*, 1991]. The amplitude to wavelength ratio α of these surfaces lies between 10^{-3} and 10^{-2}, the lower limit being more representative of mature faults [*Power and Tullis*, 1991], and this is independent of scale. *Sagy and Brodsky* [2009] suggest that the value of α decreases as faults mature due to wear processes. In this study, we generate a fault having α 0.005 and minimum roughness wavelength of 60 m. A mathematical description for generating rough fault profiles is discussed in *Dunham et al*. [2011b]. Stress perturbations caused by the roughness impact the rupture propagation by introducing heterogeneities in the slip distribution and cause rapid accelerations and decelerations at the rupture front [*Dieterich and Smith*, 2009].
3. *Background stresses*: Next, the model described above is loaded with a reverse faulting stress state. The maximum horizontal stress and the vertical stress are assumed to be the maximum and minimum principal stresses, while the minimum horizontal stress lies in the plane of the fault. The stress field applied is depth dependent. The total vertical stress gradient is 23 MPa/km (obtained from density logs), while the pore pressure is 12 MPa/km (interpreted from drillstem test data).
4. In this study, we assume that ruptures propagate as self-sustaining pulses. Since pulses propagate only at a very narrow range of background shear stresses (or a narrow range of the ratio between shear to normal stresses resolved on the fault plane), it is possible to constrain the maximum horizontal principal stress at which slip nucleates given the vertical stress. The magnitude of the maximum horizontal stress is assumed to be the minimum stress at which the resolved shear to effective normal stress ratio (τ/σ_n) on the fault is barely sufficient to cause a rupture to propagate as a self-healing pulse. For the parameters used to define the strongly rate-weakening friction law chosen in this study, the value of τ/σ_n is 0.336 for a planar fault and 0.3476 for a nonplanar fault. These values are far less than the levels conventionally assumed in rupture modeling [e.g., *Harris et al*., 2009]. This might suggest that the stresses in Earth's crust should not build up to larger levels. However, fault roughness on nonplanar faults introduces an additional resistance to slip (roughness drag) due to which larger values of τ^{pulse}/σ_n (depending on the amplitude to wavelength ratio α and the local slope of the fault at the nucleation point) would be required to propagate the rupture as a pulse [*Fang and Dunham*, 2013]. In the present study, for a vertical stress gradient of 23 MPa/km, the maximum principal stress gradient calculated from the appropriate τ/σ_n is 33.6 MPa/km for a planar fault and 34.04 MPa/km for a nonplanar fault. The initial out-of-plane normal stress (minimum horizontal stress) is taken to be the average of the two in-plane normal stresses (following *Templeton and Rice* [2008]). This stress component is only relevant during plastic flow. For this assumption, the Drucker-Prager yield function coincides with the Mohr-Coulomb condition. However, this correspondence ceases once plastic flow commences.
5. *Simulation details and input parameters*: A 2-D finite difference method is used to model the dynamic rupture propagation. This is done in the framework of continuum plasticity. The governing equations are written as a system of first-order partial differential equations with an algebraic constraint. The structured mesh discretizes the medium keeping the grid spacing approximately 1 m in both directions. All components of velocity and stress are defined at each grid point. Spatial derivatives are approximated using a summation by parts finite difference method [*Kreiss and Scherer*, 1974, 1977; *Strand*, 1994; *Mattsson and Nordström*, 2004].

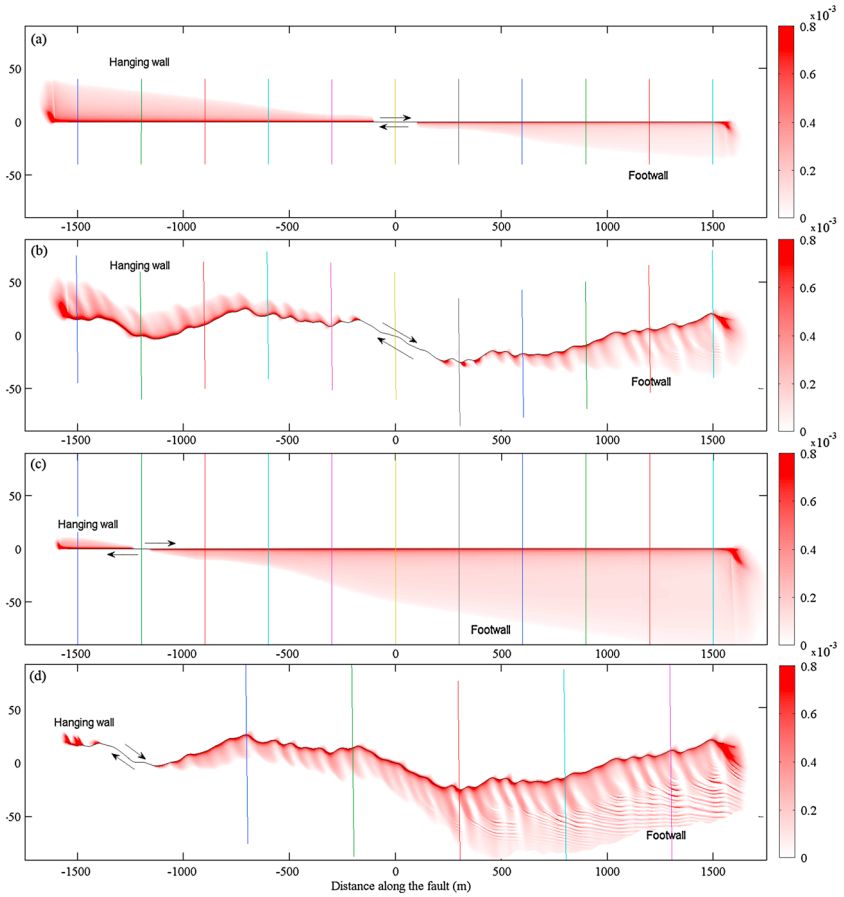

Figure 3. Equivalent plastic strain field generated during dynamic shear rupture. (a and b) Ruptures that nucleate at the fault center (origin) and propagate bilaterally on planar and nonplanar faults, respectively. (c and d) Ruptures that nucleate close to the lower end of a planar and nonplanar fault and propagate unilaterally. These 30° dipping planes have been rotated clockwise to lie along the *x* direction. The vertical lines represent transects along which we study plastic strain and fracture density variation. (All dimensions are in meters) Volumetric plastic strains are obtained as a product of dilatancy and shear plastic strains. Vertical exaggeration is in scale of 2.7.

The boundary conditions are weakly enforced using the simultaneous approximation term technique [*Carpenter et al.*, 1994]. This scheme is high-order accurate [*Kozdon et al.*, 2012]. For more details on the numerical method and simulation process, please refer to *Dunham et al.* [2011a] and *Kozdon et al.* [2011, 2012]. Table A1 in Appendix A1 lists the values of various model parameters used in the simulations. The parameters of the friction law are similar to those used by *Noda et al.* [2009] who selected them from a compilation of laboratory studies. The time step in the flat fault and rough fault simulations is 40 μs and 20 μs, respectively.

6. *Arresting a propagating rupture*: Ruptures propagating on a fault may arrest due to several reasons such as end of a fault surface, fault intersection, or unfavorable fault geometry. Arresting the rupture abruptly generates large plastic strains. This is an artifact of the sudden stoppage of the rupture that creates large stress perturbations. Evidence from seismic inversions suggests that the rupture arrest process is gradual. We try to mimic a gradual rupture arrest process by ramping up the value of the direct effect parameter *a* to values larger than the evolution effect parameter *b* gradually over a spatial distance of 80 m. Ramping up the *a* value gradually transforms the friction law from rate weakening to rate strengthening. This arrests the rupture gradually over a relatively large distance and prevents the generation of unreasonably large stress perturbations and plastic strains.

5. Results

Please note that although most results shown below and the distinctions made in terms of differences in damage zone attributes in the hanging wall and footwall are general, others may be specific to thrust faults that we have modeled in this study.

1. *Slip-induced inelastic deformations*: As a rupture propagates, it deforms the rock around the propagating rupture front inelastically. A discussion on the mode of rupture propagation and fault slip profiles is provided in Appendix B. Here we will only focus on inelastic deformations due to rupture propagation. Figures 3a and 3b show the equivalent plastic shear strain field generated due to shear ruptures on planar and nonplanar faults that nucleate at the center of the fault and propagate bilaterally, while Figures 3c and 3d represent the plastic strain field generated due to unilaterally propagating ruptures on planar and nonplanar faults that propagate in the updip direction. Equivalent plastic strain γ^P is related to the equivalent plastic strain rate λ as $\lambda = \mathrm{d}\gamma^P/\mathrm{d}t$ where $\lambda = \sqrt{2\dot{e}_{ij}^p \dot{e}_{ij}^p}$ and $\dot{e}_{ij}^p$ is the deviatoric plastic strain rate. λ is a scalar measure of the shear plastic strain rate. The fault dips at 30°, but the plot has been rotated by 30° in the clockwise direction so that the fault surface is aligned with the *X* axis (Figure 2). We consider this region undergoing inelastic deformations the damage zone formed due to slip on the fault.

   The plastic strains are mostly limited to the extensional stress quadrants with respect to the slip mode on the fault. This is in accordance with *Templeton and Rice* [2008], who have shown that the region undergoing inelastic deformation around a propagating crack tip depends on the angle ψ between the fault plane and the direction of maximum principal stress. For ψ less than 20°, the inelastic deformation occurs primarily in the compressional quadrants, while for ψ larger than 45°, the inelastic deformation occurs exclusively in the extensional quadrants. For angle ψ of 30° as used in this study, the inelastic deformation occurs primarily in the extensional quadrants. We also notice that the equivalent plastic strain field is relatively uniform for a planar fault as compared to a nonplanar fault where the plastic strain field is strongly modulated by the fault nonplanarity [*Dunham et al.*, 2011b]. Figure 3 also shows transects perpendicular to the fault surface along which we study the variation of plastic strains and fracture density. These transects are located at 300 m, 600 m, 900 m, 1200 m, and 1500 m from the point of nucleation for bilaterally propagating ruptures and at 500 m, 1000 m, 1500 m, 2000 m, and 2500 m from the base of the fault for the unilaterally propagating ruptures.

   Figure 4 shows the spatial extent of plastic strains generated from the surface of faults. The *X* axis represents the distance along the fault with positive values indicating the fault surface above the center of the fault. The *Y* axis represents the perpendicular distance from the fault up to which finite plastic strains (damage) are generated. Figure 4a represents the extent of finite plastic strains (inelastic deformations) for bilaterally propagating ruptures that nucleate at the origin, while Figure 4b represents the extent of plastic strains around ruptures that nucleate close to the lower extreme of the fault and propagate unilaterally, primarily in the updip direction. Blue lines represent the extent of plastic strains from the fault due to rupture propagation on a planar fault, while the red lines represent those due to propagation on a nonplanar fault.

   From both the plots, we notice that the extent of inelastic deformations increases with propagation distance (distance from the point of nucleation) for both planar and nonplanar faults. A similar phenomenon has also been reported by *Andrews* [2005], *Yamashita* [2000], *Dalguer et al.* [2003a, 2003b], and *Templeton and Rice* [2008] but for cracks. The reason emerges out of self-similarity of the propagating rupture. The crack length or the size of the slip pulse increases linearly with propagation distance. This results in a linear increase of the energy release rate with propagation distance. The energy release rate is balanced by the fracture energy, which has two contributors, frictional weakening on the fault and energy dissipated due to plastic deformation. In our simulations, contribution from plastic deformation dominates; therefore, the amount of net plastic strains adjacent a particular section of the fault increases linearly with propagation distance. However, since the magnitude of plastic strain almost remains constant, the extent of inelastic deformation from the fault increases linearly with propagation distance. (Please note that in Figure 4, the extent of damage at values of *X* to the right of the nucleation point represent the damage in the footwall, while those on the left represent damage in the hanging wall of the modeled thrust fault.) Consequently, for a fault of a certain size, unilateral ruptures can achieve larger propagation distances resulting in a larger region deforming inelastically. Therefore, damage zones modeled due to a single rupture are spatially heterogeneous, their widths increasing linearly with distance from the nucleation point. However, we will see later that this variability gets homogenized when we consider the effect of multiple slip events uniformly distributed on the fault plane.

   For ruptures propagating on nonplanar faults, stress perturbations caused by fault roughness impact the rupture propagation by introducing heterogeneities in the slip distribution, stress heterogeneities that affect the occurrence of plastic strain, and rapid accelerations and decelerations of the rupture front. From the red

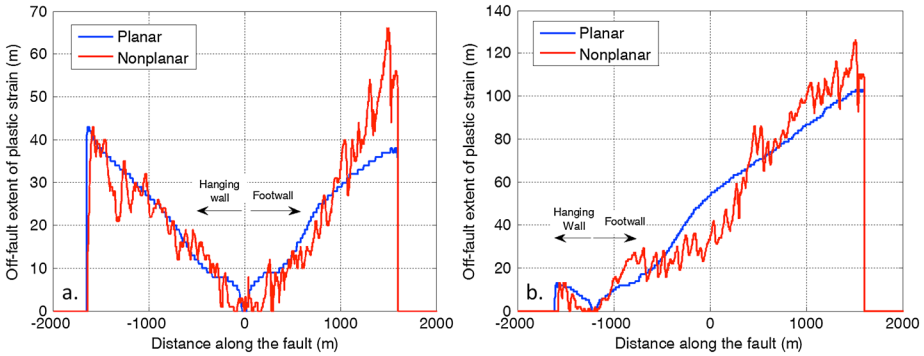

Figure 4. Extent of damage from the surface of a planar fault versus a nonplanar fault. The damage zone at points above the nucleation point (points to the right of the nucleation point in the plots above) is present in the footwall while that below the nucleation point is in the hanging wall.

lines in Figure 4, we see that the local fault roughness modulates the extent of inelastic deformations from the fault. This leads to short wavelength variations in the extent of the inelastically deforming region. However, the overall trend of increasing off-fault extent of plastic strains with propagation distance holds.

2. *Converting plastic strains to fractures*: So far, we have obtained continuum plastic shear and volumetric strains generated in the material surrounding the fault on which the rupture propagates. However, our objective is to compare model results (obtained in continuum) with damage zones observed around faults (M. Johri, submitted manuscript, 2012) which are quantified in terms of fracture density (number of fractures per unit length). Therefore, we are required to convert dilatant plastic strains to fractures. We assume that the entire volume created by dilatant plastic strains is manifested completely in the form of macrofractures. As mentioned earlier, the structured mesh discretizes the medium keeping a grid spacing of about 1 m × 1 m. We consider a cubic volume element of dimension h around each grid point and assume the plastic strain present at that grid point to be representative of the plastic strain in this unit volume (Figure 5).

   Total volume created by plastic strains in this cubic volume = $\beta\gamma^p h^3$ where β is the dilatancy and γ^p is the shear plastic strain.

   Assuming the average fracture dimension inside this cubic volume to be h^2, the average volume of a fracture inside the cubic volume = aperture × h^2

   Therefore, number of fractures in the cubic volume = ($\beta\gamma^p h^3$)/ (aperture × h^2) = $\beta\gamma^p h$/aperture

   Hence, fracture density = ($\beta\gamma^p$/aperture) fractures per meter. The result is thus independent of the spatial discretization h.

   Dilatancy is defined as the change in volume resulting from the shear distortion of material element. Dilatancy can mathematically be expressed as sin(ϕ) where ϕ is the dilatancy angle. Assuming a dilatancy angle of 15° [*Alejano and Alonso*, 2005], we obtain a dilatancy of 0.26.

   Several studies report experimentally observed values of average fracture apertures [*Esaki et al*., 1999; *Chen et al*., 2000; *Lee and Cho*, 2002]. Morphological analyses of fracture surfaces show prominent surface undulations [*Giacomini et al*., 2007]. This leads to a spatially heterogeneous aperture distribution over the fracture surface. Studies also suggest that the fracture surface aperture distribution could be approximated by a normal distribution (*Hakami* [1995] for the case of natural fractures, *Esaki et al*. [1999] for artificially created tensile fractures, and *Lee and Cho* [2002] for tensile fractures in granite). Therefore, in the absence of a unique fracture aperture value, an equivalent mechanical aperture is measured by various methods such as using gas to measure fracture volume [*Chen et al*., 2000]. These studies also show that the mechanical aperture of fractures is sensitive to shear displacement across fractures and the confining pressure. For confining stresses between 6.9 MPa and 34.5 MPa (which includes the range of normal stresses acting on fractures in our region of study) and shear displacement of 0.5 mm across fractures (we assume a modest shear slip assuming fractures formed are shear fractures with a finite shear displacement), the average mechanical aperture experimentally reported is approximately 0.1 mm [*Chen et al*., 2000].

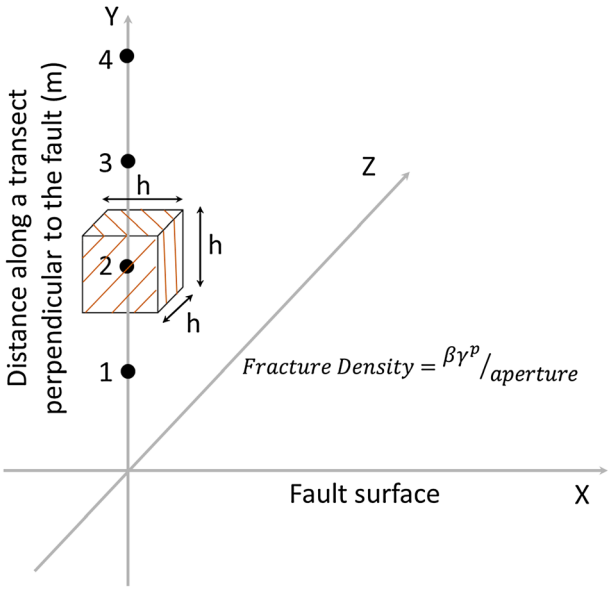

Figure 5. Conversion of plastic strains to fracture intensity. Volume created by dilatant plastic strain inside the cubic volume is assumed to be manifested completely in the form of fractures. By making reasonable assumptions of fracture dimensions, the fracture density at various points can be calculated.

Following this methodology helps us compute the spatial distribution of fracture intensity created by slip on the fault. Although the magnitude of fracture density is dependent on our assumption of mean fracture aperture, the relative fracture density at various points around the fault is independent of this assumption. We will see later in the paper that since we calibrate our model by matching the absolute magnitude of fracture density observed in the SSC reservoir data set, our assumption on the mean fracture aperture does not have much consequence.

Ideally, we should consider the partitioning of dilatant plastic strains into both microfractures (characteristic length scale in millimeters) and macrofractures (characteristic length scale in meters), but since our ultimate objective is to study the large-scale permeability anisotropy introduced by damage zones, we will only limit our analysis to macrofractures.

3. *Decay of fracture density with distance from the fault*: Adopting the above methodology, we calculate the fracture density along various transects perpendicular to the fault and study its variation with distance from the fault. Figure 6 shows this variation in the damage zone resulting from a bilaterally propagating rupture that nucleates at the center of a planar fault. The transects are selected at distances 300 m, 600 m, 900 m, 1200 m, and 1500 m from the point of nucleation (Figure 3a). As mentioned previously, the peak fracture density and damage zone width increase with propagation distance. However, there is also a subtle dependence of damage zone widths on depth (since depth-dependent stresses are considered, greater stress drops are produced at larger depths leading to larger energy dissipation and width of damage zones). These two variables compete against each other in the footwall since propagation distance increases with decreasing depth. As a result, the fracture decay profiles significantly overlap in the footwall, as opposed to those in the hanging wall which are fairly distinct. Both the propagation distance and depth coincrease in the hanging wall leading to explicitly larger fracture density and damage zone widths at larger distances from the point of nucleation.

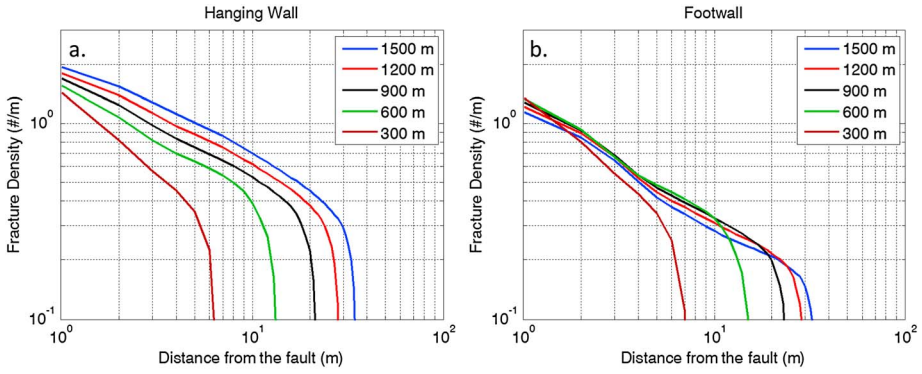

Figure 6. Fracture decay profiles in the damage zone in the hanging wall and footwall. The damage zone modeled is due to a bilaterally propagating rupture which nucleates at the center of a planar fault. Various colors represent transects at various distances from the nucleation point.

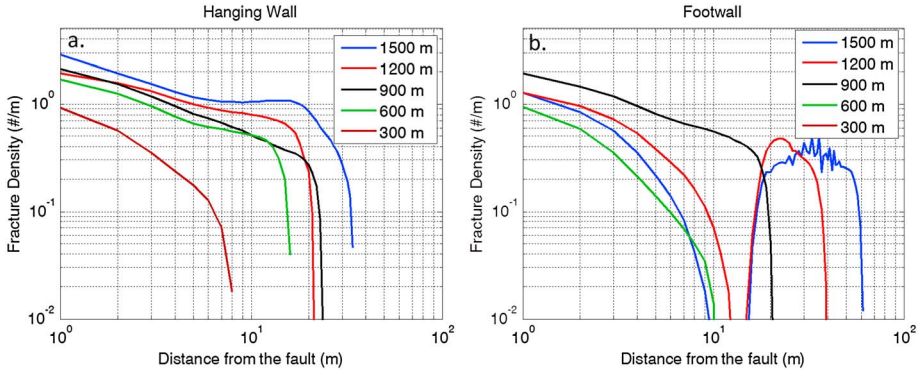

Figure 7. Same as Figure 6 but for a nonplanar fault.

The width of the damage zone ranges from 6 to 40 m in both the hanging wall and the footwall with the damage zone being wider farther away from the point of nucleation. These are considerably narrower than 50–80 m wide damage zones reported by (M. Johri, submitted manuscript, 2012) using image log observations.

The fracture decay rate can be described by a power law. The rate of decay (value of n in the power law described by $F = F_0 r^{-n}$ where F is the fracture density at r meters from the fault, F_0, also known as the fault constant, is the fracture density at 1 m from the fault) ranges from 0.51 to 1.06, larger decay rates being closer to the point of nucleation. This range of decay rates is similar to that reported from field observations by (M. Johri, submitted manuscript, 2012) and outcrop studies [*Savage and Brodsky*, 2011]. Previous studies have suggested a logarithmic [*Chester et al.*, 2005] or exponential [*Mitchell and Faulkner*, 2009, 2012] decay of fracture density with distance from the fault. While an exponential decay implies a characteristic length scale, a true power law does not. Simulations in this study show power law behavior within the damage zone and then an abrupt cutoff, so it has features of both a true power law and an exponential decay.

Although the actual number of fractures computed is dependent on our assumption of the mean fracture aperture, the width of damage zones and the fracture density decay profiles are independent of that assumption. Fracture density in this paper is computed assuming a mean fracture aperture of 100 μm. A different assumption would only change the fracture density, but not the decay rate and extent of damage from the fault. The fault constant computed assuming an average aperture of 100 μm is approximately 1–2 fractures/meter. This is lower than that reported by (M. Johri, submitted manuscript, 2012) (approximately 8–20 fractures/meter). Outcrop studies suggest that the fault constant may have a wide range of values depending on the lithology and the amount of slip across the fault [*Savage and Brodsky*, 2011], but in general, they are larger than what our single-event model predicts. The above results also suggest a spatial variability in the width of damage zones which is inconsistent with field observations. There are two possible explanations for such discrepancies, first the assumption of a single event (damage zones are a result of the cumulative effect of several slip events) and second our assumption of fracture aperture. Accounting for several slip events in order to reconcile with the above discrepancies is discussed in the next section.

Figure 7 shows the fracture decay profiles in the damage zones of the hanging wall and the footwall formed due to a rupture propagating bilaterally on a nonplanar fault. The fault constant in both the hanging wall and the footwall is approximately 1–3 fractures/meter. Although the trend of increasing damage zone width and fracture density with depth and propagation distance still holds in general, fault roughness disturbs the trend. From Figure 7a we notice that unlike in the case of planar faults, the decay rate in the damage zones in the hanging wall is not constant, especially at larger distances from the nucleation point as seen for the transect at 1500 m. Damage zone in the footwall (Figure 7b) is even more complex where the fracture decay rate is not even monotonic at larger distances (transects at 1200 and 1500 m) from the nucleation point. The fracture density first monotonically decreases with distance from the fault then increases again before plummeting. This is the result of severe strain heterogeneity and variability. Figure 3b shows the transects at 1200 and 1500 m from the nucleation point in the footwall to be traversing across a very heterogeneous strain field which produces a fracture density decay profile as seen in Figure 7b. The fracture decay profile at 300 m in Figure 7b is not shown as there is no plastic strain produced along the entire transect (Figure 3b). The fracture density decay rate in regions where it

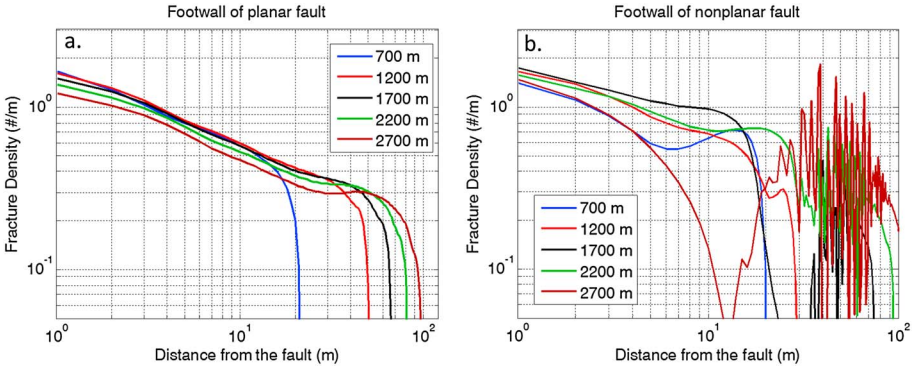

Figure 8. Fracture decay profiles in the damage zone modeled formed by to a unilaterally propagating rupture which nucleates close to the lower tip of a (a) planar and (b) nonplanar fault. Various colors represent transects at various distances from the nucleation point. Damage zone in a unilaterally upward propagating thrust fault are primarily restricted to the footwall.

decreases monotonically continues to lie between 0.5 and 1 (similar to that for planar faults). Overall, fracture density decay for a nonplanar fault can no longer be explained accurately by a power law or any other mathematical law due to a strong heterogeneity arising from local fault roughness.

Damage zones modeled around nonplanar faults are approximately 10–60 m wide and include regions with a nonmonotonic fracture decay and buildup. Although the damage zone attributes such as width, fault constant, and fracture decay rates are sensitive to the local fault roughness, on average these attributes are of the same order of magnitude as those derived from modeling damage zones around planar faults.

Figure 8 shows the fracture decay profiles in the damage zones modeled due to an upward unilaterally propagating rupture. The damage zone due to such a rupture is restricted primarily to the footwall of the thrust fault. Figure 8a represents transects in the rupture-induced damage zone around a planar fault, while Figure 8b represents those around a nonplanar fault. In case of a planar fault (Figure 8a), the fault constant is approximately 1–2 fractures/meter (similar to that obtained in damage zones modeled around bilaterally propagating ruptures). Damage zone becomes wider with increasing propagation distance and are as large as 60–100 m. This happens because larger propagation distances can be achieved for ruptures propagating unilaterally on a fault of a certain length. The above argument may imply a direct scaling between damage zone width and fault length. Field observations suggest that such a scaling between damage zone width and fault size does exist up to a certain threshold fault size of approximately 2400 m, beyond which the width of damage zone saturates [*Mitchell and Faulkner*, 2009; *Savage and Brodsky*, 2011]. However, since we are only dealing with relatively smaller, reservoir-scale, second-order faults, such a scaling should hold. The fracture density decay can again be explained by a power law with the decay rate approximately between 0.5 and 1.

The fracture density decay profiles in the damage zone around a unilaterally upward propagating nonplanar fault are, as expected, not monotonically decreasing (Figure 8b). From Figure 3d which represents the equivalent plastic strain field produced due to such a rupture, we notice very fine strain localizations especially after 1500 m of propagation ($X > 500$ m). This produces extremely short wavelength variations in fracture density as seen in Figure 8b, especially at larger distances (transects at 2200 and 2700 m) from the nucleation point. Essentially, these variations become more pronounced in those parts of the damage zone which are adjacent to sections of the fault at larger distances from the nucleation point, as these regions have a greater population of strain localization features (Figure 3d). The fault constant is approximately 1–2 fractures per meter in damage zones that are 20–100 m wide—very similar to those around planar fault. So, although it is difficult to explain fracture density decay profiles and damage zone widths around nonplanar faults mathematically, we can still obtain an idea of effective or approximate damage zone attributes.

4. *Mathematical calibration and consideration of multiple slip events*: Fault damage zones observed in nature are the cumulative product of multiple slip events that the faults have hosted over geologic times. So far we have only considered a single slip event. Results from such modeling (previous section) suggest that the width of damage zones and rate of fracture density decay inside damage zones are consistent with those observed in image logs (M. Johri, submitted manuscript, 2012) and those reported from field studies [*Mitchell and Faulkner*, 2009; *Savage and Brodsky*, 2011]. The prominent difference, however, is in the

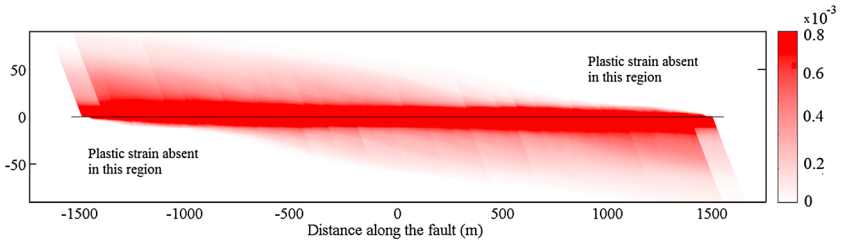

Figure 9. Equivalent plastic shear strain field obtained by superposition of the plastic strain fields caused by multiple slip events on a planar fault. (All dimensions are in meters) Volumetric strains are obtained as a product of dilatancy and shear plastic strains. Vertical exaggeration = 4.7. The width of damage zone relatively gets homogenized. Plastic strain concentration near the fault gets enhanced.

values of fracture density, where fracture density in the modeled damage zones is significantly lower. The uncertainty in fracture density arises out of uncertainty in mean fracture aperture (which is an inherent problem in transforming from continuum to discrete space) and the cumulative effect of multiple slip events in shaping fault damage zones. Besides, there is also a systematic spatial heterogeneity in the width of damage zones which is inconsistent with field observations.

The issue of considering the cumulative effect of multiple slip events adds complexity. While it may be possible to model the cumulative effect of multiple earthquakes more accurately by quantifying the probability of various potential nucleation sites hosting a rupture, using data on background seismicity and earthquake cycles to estimate the frequency of rupture events, and modifying surrounding rock material properties after each slip event, we have adopted a simplified approach. In order to reconcile with the uncertainty pertaining to multiple slip events, we superimpose plastic strains generated due to multiple slip events assuming that the residual stress field left by one rupture has negligible influence on the occurrence of plastic strain in subsequent events. The number of these slip events is obtained by calibrating the model as explained below.

Faults in nature have hosted many slip events of various magnitudes in the geologic past. It is reasonable to assume that the number of earthquakes of certain magnitudes that a fault has hosted scales with the magnitude in accordance with the Gutenberg-Richter law. The law expresses the relationship between the magnitude and total number of earthquakes in any given region and time period of at least that magnitude as $\log_{10} N = a - bM$ where N is the number of events having a magnitude $\geq M$ and a and b are constants (constants a and b are distinct from the constants used to describe the rate and state friction). The constant b is approximately equal to 1.0 in seismically active regions. We consider earthquakes ranging from magnitude 1 to magnitude 5.2 to have been hosted on the fault. The upper limit ($M = 5.2$) is constrained by the largest magnitude earthquake that a 3 km long fault can host (scalar seismic moment $M_0 \approx \Delta\sigma \times l^3$ where l is the fault length and $\Delta\sigma$ is the stress drop, a reasonable assumption of the stress drop is ~ 2 MPa [*Allmann and Shearer*, 2009]; magnitude $Mw = 2/3 \log M_0 - 6.03$ in SI units) while the lower limit ($M = 1$) is constrained by our choice of earthquake size that would create a damage zone whose width is the lower limit of damage zone widths we wish to consider in this study. Let us suppose we are interested in those slip events which at least create a 1 m damage zone. Since rupture propagation and the plastic strain field they create are self-similar, we can argue that if a 3000 m long rupture creates a damage zone that has a maximum width of 110 m (Figure 9), slip on a 3000/110 = 27.27 m long fault patch would create a damage zone that has a maximum width of 1 m. An earthquake on a fault segment 27.27 m long would approximately be a magnitude 1 earthquake.

The unconstrained parameter a in the above formulation is what we use to calibrate the model. For any value of a, we get a distribution of slip events of various magnitudes from the Gutenberg-Richter law. Magnitudes of plastic strains generated around the fault are independent of propagation distance while the extent of plastic strains from the fault scales with propagation distance. Therefore, the plastic strain field created due to a small event is obtained by downscaling the spatial distribution of the plastic strain field (but not the magnitudes) obtained around a 3 km long rupture to that around a small fault segment. For example, the plastic strain field ε_l^p around a fault of length l can be computed from the plastic strain field ε_L^p produced around a fault of length L. The plastic strain at a distance x from the point of nucleation

and a perpendicular distance *y* from the surface of a fault of length *l* [i.e., $(\varepsilon_l^p(x,y))$] would be equal to the plastic strain at a distance *Lx*/*l* from the point of nucleation and a perpendicular distance *Ly*/*l* from the surface of the fault of length *L* [$\varepsilon_L^p(xL/l, yL/l)$], i.e., $\varepsilon_l^p(x,y) = \varepsilon_L^p(xL/l, yL/l)$. By superimposing the plastic strain field due to all the events and converting the net plastic strains into a fracture population, we obtain the damage zone attributes. We calibrate our model by placing the constraint that the fault constant predicted by our model should be equal to that suggested by field observations. *Savage and Brodsky* [2011] have compiled data from various published studies and reported that although in general there exists no clear relationship between displacement across the fault and fault constant, there appears to be a trend between the two parameters for siliciclastic sedimentary host rocks. In this lithology, the fault constant increases with displacement until approximately 150 m and then remains constant. This is expected since there is an upper limit for fracturing beyond which there is complete damage and cataclasis. A similar relationship also holds for igneous rocks [*Faulkner et al*., 2011] that largely constitute the SSC reservoir. A good estimate of displacement across reservoir-scale faults can be obtained from seismic images. For model calibration purposes, we choose that value of *a* which gives an earthquake magnitude number distribution such that the plastic strain field obtained by the superposition of the individual event plastic strains produces a fault constant that matches the one given by this trend from field observations.

Seismic images from the SSC reservoir show that the displacement across various reservoir-scale faults lies between 8 and 180 m. For example, if we consider a specific fault with a displacement of 20 m, the scaling relationship suggests that the fault constant should be approximately 20 fractures/meter. Model calibration involves choosing an "*a*" value such that the net plastic strain field translates into an approximate fault constant of 20 fractures per meter. The estimated value of *a* in this case is ~ 6.6. If we consider a fault with a different displacement, the scaling relationship would point toward choosing a different *a* value.

Please note that if the Gutenberg-Richter law suggests *n* number of earthquakes within a certain magnitude window, we can assume the events to be uniformly distributed on the fault plane. However, since we are using a two-dimensional model in which a fault is modeled as one-dimensional, the number of earthquakes within that magnitude window occurring on the 1-D fault would be $\sqrt{n}$.

5. *Nucleation points for various slip events*: The nucleation points for various slip events obtained from the previous step are required to be constrained. Nucleation points are points on the fault surface where ruptures start and are thought to be localized regions where conditions are most favorable to slip. Various factors that create a conducive nucleation environment include locally elevated pore pressures, fault geometry effects that locally increase the shear to normal stress ratio, localized geochemical and lithology effects that locally decrease fault friction, etc. In the present study, we adopt a simpler approach. The number of slip events of various magnitudes and hence the number of events occurring on fault segments of various lengths are obtained from the previous step. We choose both the fault segment on the main fault and the nucleation point on that fault segment randomly assuming a uniform distribution.
6. *Damage zones resulting from the cumulative effect of multiple slip events*: The equivalent plastic strain field obtained after superimposing plastic strains due to multiple events as described in the previous section is shown in Figure 9. It is clear that the variability in the widths of damage zones modeled due to a single rupture gets homogenized. Besides, considering a power law event size distribution (Gutenberg-Richter law) enhances the plastic strain concentration near the fault due to a very large number of relatively small-magnitude events that produce small damage zones.

Figure 10 shows the width of the damage zone at various positions along the fault. The *X* axis represents the fault surface. The spatial variability in the width of damage zones modeled due to a single slip event gets homogenized by considering the cumulative effect of several events uniformly distributed along the fault. The damage zones modeled are approximately 60–100 m wide in most regions.

Figure 11 shows the fracture decay profiles along various transects in the modeled damage zones. The decay of fracture density in both the hanging wall and footwall seems to follow power law decay. For reference, the red dotted line represents a power law decaying at a rate of 0.8. The modeled fracture density inside damage zones appears to be decaying at this rate up to 10 m from the fault, after which the decay rate increases. This happens due to the concentration of plastic strains close to the fault resulting from a relatively large number of small-magnitude slip events.

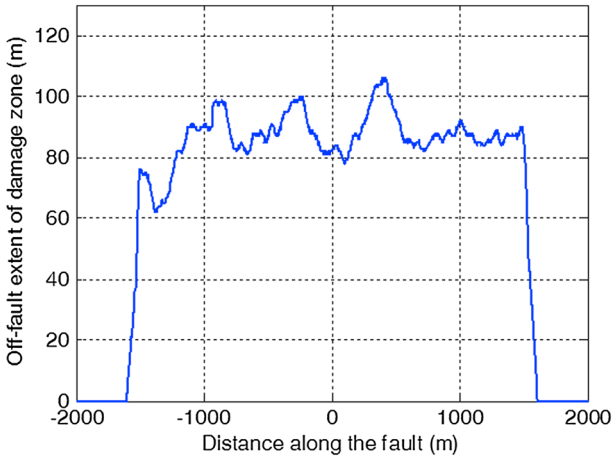

Figure 10. Damage zone modeled around a planar fault as a cumulative effect of multiple slip events. The *X* axis represents the fault surface. The effect of superpositioning is the homogenization of the spatial variability in the width of damage zones. The damage zone is approximately 60–100 m wide.

Damage zone attributes modeled are very similar to those reported from field observations using image logs (M. Johri, submitted manuscript, 2012). Their study reports 50–80 m wide damage zones. In their study, damage zones in the SSC reservoir are characterized by decay rates ranging from 0.68 to 1.06 (with an average of ~0.8), while those in the arkosic section show slightly gradual decay rates lying between 0.4 and 0.75 (an average of ~0.56). Based on compilation of results from several outcrop studies, *Savage and Brodsky* [2011] suggest fault zones 50–80 m wide around faults with a fault displacement between 30 and 60 m (which is the displacement across the faults in the SSC reservoir that we are modeling). They also suggest that the fracture density decay inside damage zones can be described by a power law with an average decay rate of approximately 0.8. These observations are consistent with the 60–100 m wide damage zones that we have modeled in which the decay rate is approximately 0.85 up to a distance of 10 m after which it increases at a greater rate. The 60–100 m wide damage zones modeled around a 3000 m long fault are also consistent with the fault size damage zone width scaling suggested in *Mitchell and Faulkner* [2009].

The damage zones modeled in this study are around a 3000 m long fault. Invoking self-similarity of rupture propagation for second-order faults, we can say that the modeled width of damage zones scales with fault size. The maximum width of the damage zone scales with propagation distance of the largest ruptures, which is, in fact, a measure of the fault size. Therefore, it is important to note that the width of damage zones modeled depends on the fault size and can be estimated if the fault size (which can be constrained from seismic images) is known. The scaling of damage zone widths with fault size, however, does not hold for large first-order faults since damage zone widths saturate beyond a certain fault size (due to the limited thickness of the seismogenic zone). *Faulkner et al.* [2011] also consider the effect of multiple ruptures on the development of damage zones and compare them with data from low-displacement faults in crystalline rocks. They conclude that the scaling from field observations could, in fact, be explained by multiple ruptures if the size of ruptures increases with increasing fault length, similar to the conclusions of this study. The results presented here account for multiple slip events on a planar fault. We have omitted results for a nonplanar fault since introducing fault roughness does not significantly affect the modeled damage zone attributes.

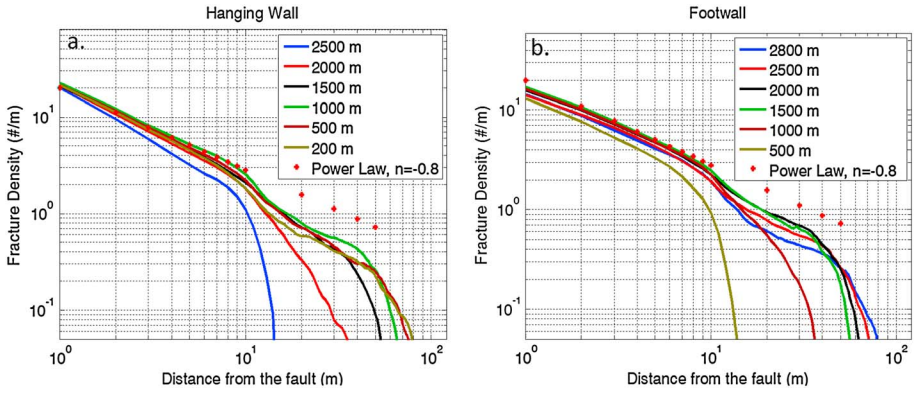

Figure 11. Fracture decay profiles in the (a) hanging wall and (b) footwall of the damage zone modeled. Various lines represent fracture density decay profiles across transects at the mentioned distances from the base of the fault. Dots represent a power law decay (decay rate of 0.8) reported for damage zones identified in the SSC reservoir using image logs (M. Johri, submitted manuscript, 2012).

The above methodology requires a model calibration step to fix the *a* value in the Gutenberg-Richter law. The chosen *a* value depends on the target fault constant. Therefore, if we can obtain the value of the fault constant of the fault (either from image logs or scaling relationships between fault constant and fault displacement), we can constrain and predict the remaining attributes of damage zones, namely, the damage zone widths and the spatial variability of fracture density with distance from the fault.

6. Discussion

Various assumptions have been made in modeling damage zones and comparing these results with observations from field studies. Plastic strains obtained from modeling performed in a framework of continuum plasticity are converted into a fracture population after assuming fracture dimensions, followed by volume balancing. This is a necessary step in translating from a continuum space into a discrete space. The cumulative effect of multiple earthquakes is accounted for by calibrating the model and superimposing plastic strains from multiple slip events such that the fault constant matches that observed from field studies. The nucleation points for multiple slip events are randomly distributed using a uniform distribution, disregarding the fact that certain locations on the fault could be more likely to nucleate ruptures. Besides, subsequent slip events deform the material and alter the rock properties. This may affect rupture dynamics. Technically, we should update the material properties and keep track of accumulated deformation after each slip event. However, we assume a Drucker-Prager yield criterion. This is a shear failure criterion which assumes that fracture surfaces of all orientations are already present in the rock, and yielding results in slip of well-oriented planes. In the light of this assumption which considers predamaged rock, it may not be required to keep track of material deformation after each slip event (since it is already damaged). However, the outstanding assumption of the surrounding material being predamaged with all fracture orientations needs to be reconciled with. This may be true if we consider the damage due to deformation processes prior to and during the fault formation stage. Prior to the stage when faults become capable of hosting earthquakes, various deformation processes could inherently damage the rock. Perhaps, larger fractures form later when faults become capable of hosting earthquakes leading to the formation of the observed character of damage zones.

In this study, we have assumed a preexisting fault on which dynamic rupture simulations have been performed. In order to account for the effect of multiple slip events, ruptures of various magnitudes are uniformly distributed on the fault and their individual plastic strain fields are superimposed. However, in doing so we ignore the stages that involve fault formation. Large-scale faults perhaps form as a result of interaction between multiple small faults. In the initial stages of fault formation, the small fault slip giving rise to small-magnitude events and the associated damage zone (in the extensional quadrant). Fractures formed at the tips of small faults (commonly referred to as wing cracks) may link the relatively close fault segments (for example, the adjacent faults in case there is an en echelon pattern of small faults) leading to fault growth. Size of events hosted by faults is constrained by fault size. As the fault size increases, they become capable of hosting larger-magnitude events. In our model, we are superimposing plastic strains due to multiple slip events of various sizes. Contribution from the smaller-magnitude events probably comes in the earlier phases of fault growth when the fault composed of smaller fault segments, while contribution from larger-magnitude events comes from progressively greater-magnitude events which occur during the latter stages of fault growth. Superimposing plastic strain fields due to multiple slip events would, perhaps, result in damage very similar to the cumulative damage around faults during fault evolution over geologic ages, the primary difference being the sequence of incremental damage accumulation.

In the process of superimposing plastic strain fields due to multiple slip events, the residual stresses are essentially ignored. The inherent assumption is that the stresses relax after a slip event and gradually begin building up over geologic time. The next rupture occurs when the stresses have built up sufficiently to create conditions conducive for slip to occur. However, it may be important to consider residual stresses because usually only certain patches of a fault slip during an earthquake. The residual stresses may not favor slip on the same fault patch but could favor slip on another fault patch which is more favorably oriented to slip under the residual stress state. Such scenarios considerably complicate the analysis and can potentially be considered in three-dimensional modeling. However, they have not been included in this study.

In this study, we have only modeled damage zone associated with relatively small, second-order, localized and isolated faults. Damage zones associated with mature faults are broader and more complex due to the presence of secondary strands that have their own loci of fracturing [*Chester et al*., 2004]. These damage zones can potentially be modeled by stochastically allowing a few fractures in the damage zone of the parent fault to become secondary strands and superimposing their respective damage zones on the parent damage zone [*Savage and Brodsky*, 2011].

This study has been limited to a homogeneous, isotropic material. It is well known that often times, a geologic fault is likely to occur on a bimaterial interface. If the material on either side of a geometrically symmetric fault is the same, with identical elastic properties and density, the change in normal stress is zero. However, if the materials across the fault have different elastic properties and density, there is a finite change in normal stress. Since the fault strength is dependent on the normal stress acting on the fault, the slip dynamics gets more complex by the coupling between slip and normal stress [*Yamashita*, 2009].

The current study also does not consider poroelastic effects. The undrained response of fluid-saturated material surrounding the fault to rapid stressing caused by rupture propagation may be strengthened or weakened against inelastic deformation. For nondilatant undrained response on the compressional side of the fault, large increase in pore pressure decreases the mean effective normal stress and weakens the material. However, positive dilatant material response on the extensional side of the fault reduces the pore pressure, increases the mean effective normal stress, and strengthens the material [*Viesca et al*., 2008]. Other than impacting the rock strength, changes in effective normal stress can also affect the rupture dynamics [*Yamashita*, 2009].

In entirety, although the present study uses a relatively simple model in comparison with the complex processes involved in rupture propagation and slip dynamics, the damage zones associated with relatively smaller, isolated second-order faults modeled closely match field observations from outcrop data and image logs. For hydrocarbon production purposes, the position of reservoir-scale faults can be constrained from seismic images and the modeling from the present study can be used to constrain the damage zone characteristics associated with these faults. This information used in conjunction with information on major fracture sets derived from image logs can assist us in building more geologically informed damage zone and fracture network models and help constrain fluid flow.

7. Conclusions

We find that damage zones associated with relatively smaller second-order buried thrust faults (~ 3000 m) can be modeled by simulating earthquake rupture events using principles of dynamic rupture propagation. Damage zones modeled as a result of a single rupture show a spatially heterogeneous character of damage zone widths along the fault length. This is a consequence of a linear scaling of damage zone width with propagation distance. The inconsistencies are resolved by considering the cumulative effect of multiple slip events of various magnitudes consistent with the Gutenberg Richter law. Such a formulation homogenizes the spatial variability in the thickness of the modeled damage zone. The modeled damage zones are 60–100 m wide. This width scales linearly with fault size. The decay of fracture intensity with distance from the fault follows power law decay. These attributes are similar to those reported in outcrop studies for similar sized faults. The modeled rate of decay is 0.85 up to a distance of approximately 10 m from the fault. The decay rate becomes sharper (~1.4) at larger distances from the fault. Such a change in decay rate can be explained by a large concentration of plastic strains close to the fault as a result of a very large number of small-magnitude events (consequence of considering a power law scaling between earthquake size and frequency). These rates are similar to those reported from field studies, although field studies do not report a break in decay rate of fracture intensity with distance from the fault. There are few field experiments that have been performed to investigate the structure of fault damage zones. Since the present study suggests an interesting change in the decay rate of fracture intensity some distance away from the fault, it could provide theoretical insights into future field studies and experiments to investigate such a change.

Fault roughness strongly modulates the local damage zone attributes, but on average, these attributes are of the same order of magnitude as those obtained for planar faults. Damage zones modeled around nonplanar faults do not strictly show a monotonic fracture density power law decay and uniform increase in damage

Table A1. Physical Properties and Model Parameters

	Material Properties	
Shear modulus	G	32.04 GPa
Shear wave speed	C_s	3.464 km/s
Poisson's ratio	ν	0.25
Drucker-Prager internal friction parameter	μ	0.5735
Drucker-Prager plastic dilatancy parameter	β	$\mu/2 = 0.2867$
	Friction Law Parameter	
Direct effect parameter	a	0.016
Evolution effect parameter	b	0.02
Reference slip velocity	v_o	1 μm/s
Steady state friction coefficient at V_o	f_o	0.6
State evolution distance	L	0.00397 m
Weakening slip velocity	V_w	0.17 m/s
Fully weakened friction coefficient	f_w	0.13
	Initial Conditions	
Vertical (min principal) stress	S_v	23 MPa/km
Maximum horizontal stress	$S_{h\max}$	21.59 MPa/km (planar fault) 22.04 MPa/km (nonplanar fault)
Pore pressure	P_p	12 MPa/km
Initial state variable	Q	0.4783
	Other	
Characteristic extent of state evolution distance	R_0	20 m

zone width with propagation distance. Since real faults are nonplanar, it is only reasonable that we consider nonplanar faults for modeling damage zones. However, in spite of the short wavelength spatial variations introduced by fault roughness, damage zone attributes modeled around nonplanar faults, on average, are similar to those modeled around planar faults at a scale (tens of meters) at which they impact bulk flow properties of damage zones and can be incorporated in flow simulators.

Appendix A: Physical Properties and Model Parameters

Table A1 lists the values of various model parameters used in the simulations.

Appendix B: Fault Slip Profiles and Mode of Rupture Propagation

We perform dynamic rupture simulations with initial conditions chosen such that ruptures propagate as self-sustaining slip pulses. Figure B1 shows the slip profile on the surface of a flat fault. The *X* axis represents the fault surface. The origin represents the point of nucleation of a bilaterally propagating rupture, and the negative and positive values represent distances (in kilometers) along the fault downdip and updip, respectively. Various lines represent slip on the fault surface at various instants of time. The shear-to-normal stress ratio required for a pulse-like rupture to propagate on a flat fault dipping at 30° is 0.336. At lower values, the rupture fails to propagate, whereas for values larger than ~0.34, the rupture propagates as a crack.

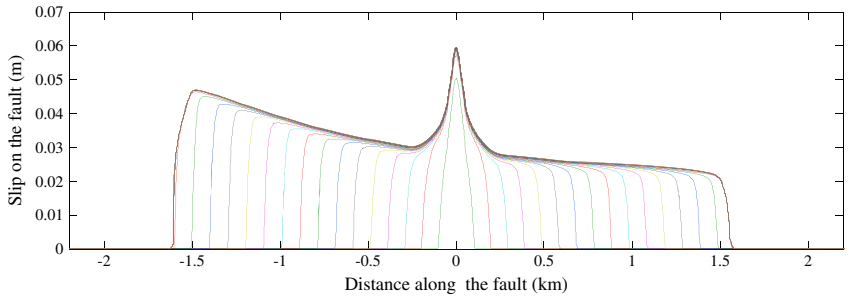

Figure B1. Plot showing the slip profile on a flat fault. Various lines represent slip profile at every 0.0347 s of rupture propagation on the fault. The origin represents the point of nucleation (depth of 2.2 km); negative *X* values represent distances downdip, while positive *X* values represent distances updip from the point of nucleation.

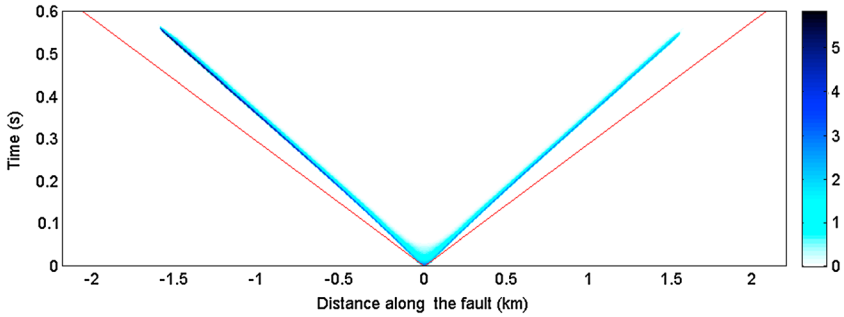

Figure B2. Plot showing the particle slip velocity (meter per second) on the fault plane at various times. The self-healing nature of the pulse propagation is clearly seen. The red lines represent the shear wave velocity, so the above is a subshear self-healing pulse-like rupture.

As noted earlier, it is only in a very narrow range of shear-to-normal stress ratios that the rupture travels as a self-healing pulse. It can be seen from Figure B1 that the amount of slip on the fault is greater downdip (~0.03–0.05 m) than updip (~0.023 m). The slip peak at the origin should be disregarded, since the increased slip is an artifact of the nucleation process.

Figure B2 shows a space-time plot of the slip velocity for the rupture on a planar fault. We notice that the center of the fault starts to slip in the beginning, but at approximately 0.05 s, it stops slipping and a finite slip velocity exists only very close to both of the rupture tips. Furthermore, the particle velocity close to the rupture tip downdip (negative values on the *X* axis) is slightly greater than updip, which could be responsible for greater stress perturbations. This also explains larger slip across the fault in the downdip direction (as seen from Figure B1).

The slip profile and space-time plot for a pulse-like rupture propagating on a rough fault are shown in Figures B3 and B4. The fault roughness (amplitude to wavelength ratio α) is 0.005, and minimum roughness wavelength is 60 m. The mathematical description of rough surfaces can be seen in *Dunham et al*. [2011b]. Roughness increases the fault's resistance to slip; therefore, larger shear stresses are required to rupture the fault. The shear-to-normal stress ratio required for a pulse-like rupture to propagate on the rough fault dipping at 30° is 0.3476. However, this value is very sensitive to the ratio of amplitude to wavelength chosen to generate the rough fault [*Fang and Dunham*, 2013]. As seen in case of a flat fault, the slip downdip is greater than updip (Figure B3). The magnitude of slip (~0.06 m downdip and ~ 0.04–0.05 m updip) is also very similar to that observed for a flat fault.

Similar to our observations for a flat fault, the center of the rough fault starts to slip during nucleation, but at around 0.1 s it stops slipping, and a finite slip velocity exists only very close to both the rupture tips (Figure B4). The particle velocity close to the rupture tip downdip (negative values on the *X* axis) is greater than updip. This leads to greater net slip across the fault in the downdip direction (as seen in Figure B3).

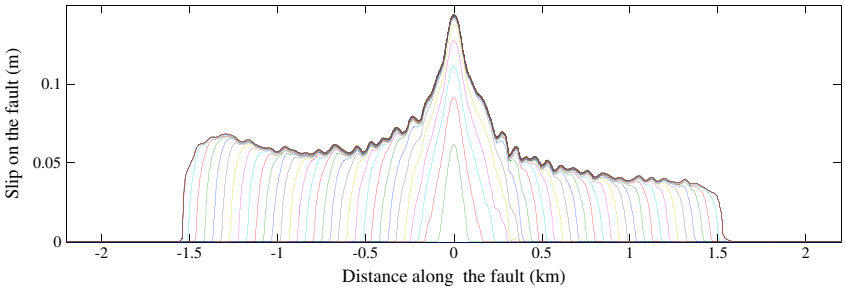

Figure B3. Plot showing the slip profile on a rough fault dipping at 30°. Various lines represent slip profile at every 0.0154 s of rupture propagation on the fault. The origin represents the point of nucleation (depth of 2.2 km); negative *X* values represent distances downdip, while positive *X* values represent distances updip from the point of nucleation.

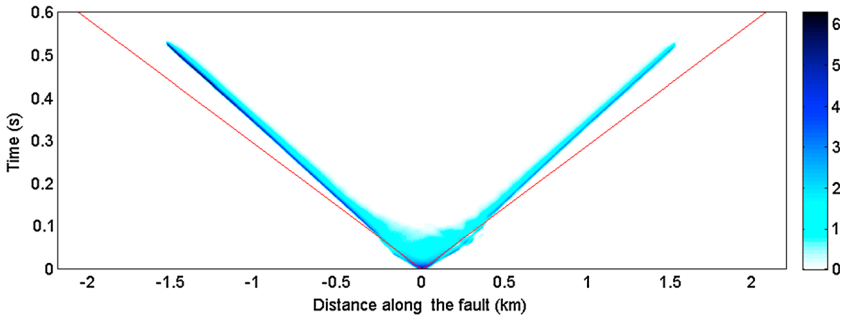

Figure B4. Plot showing the particle slip velocity (meter per second) on the fault plane at various times. The self-healing nature of the pulse propagation is clearly seen. The red lines represent the shear wave velocity, so the above is a subshear self-healing pulse-like rupture.

Acknowledgments
This work is supported by the Stanford Rock Physics and Borehole Geophysics Research Consortium. Numerical simulations were conducted at the Stanford Center for Computational Earth and Environmental Science (CEES).

References

Alejano, L. R., and E. Alonso (2005), Considerations of the dilatancy angle in rocks and rock masses, *Int. J. Rock Mech. Min. Sci.*, *42*(4), 481–507, doi:10.1016/j.ijrmms.2005.01.003.

Allmann, B. P., and P. M. Shearer (2009), Global variations of stress drop for moderate to large earthquakes, *J. Geophys. Res.*, *114*, B01310, doi:10.1029/2008JB005821.

Anderson, E. M. (1942), *The Dynamics of Faulting and Dyke Formation With Applications to Britain*, 191 pp., Oliver and Boyd, Edinburgh, Scotland.

Andrews, D. J. (1976a), Rupture propagation with finite stress in antiplane strain, *J. Geophys. Res.*, *81*(20), 3575–3582, doi:10.1029/JB081i020p03575.

Andrews, D. J. (1976b), Rupture velocity of plane strain shear cracks, *J. Geophys. Res.*, *81*(32), 5679–5687, doi:10.1029/JB081i032p05679.

Andrews, D. J. (2005), Rupture dynamics with energy loss outside the slip zone, *J. Geophys. Res.*, *110*, B01307, doi:10.1029/2004JB003191.

Beeler, N. M., T. E. Tullis, and D. L. Goldsby (2008), Constitutive relationships and physical basis of fault strength due to flash heating, *J. Geophys. Res.*, *113*, B01401, doi:10.1029/2007JB004988.

Ben-Zion, Y., and Z. Shi (2005), Dynamic rupture on a material interface with spontaneous generation of plastic strain in the bulk, *Earth Planet. Sci. Lett.*, *236*(1–2), 486–496, doi:10.1016/j.epsl.2005.03.025.

Brown, S. R., and C. H. Scholz (1985), Broad bandwidth study of the topography of natural rock surfaces, *J. Geophys. Res.*, *90*(B14), 12,575–12,582, doi:10.1029/JB090iB14p12575.

Candela, T., and F. Renard (2012), Segment linkage process at the origin of slip surface roughness: Evidence from the Dixie Valley fault, *J. Struct. Geol.*, *45*, 87–100, doi:10.1016/j.jsg.2012.06.003.

Candela, T., F. Renard, M. Bouchon, A. Brouste, D. Marsan, J. Schmittbuhl, and C. Voisin (2009), Characterization of fault roughness at various scales: Implications of three-dimensional high resolution topography measurements, *Pure Appl. Geophys.*, *166*, 1817–1851, doi:10.1007/s00024-009-0521-2.

Carpenter, M. H., D. Gottlieb, and S. Abarbanel (1994), Time-stable boundary conditions for finite-difference schemes solving hyperbolic systems: Methodology and application to high-order compact schemes, *J. Comput. Phys.*, *111*(2), 220–236, doi:10.1006/jcph.1994.1057.

Chen, Z., S. P. Narayan, Z. Yang, and S. S. Rahman (2000), An experimental investigation of hydraulic behaviour of fractures and joints in granitic rock, *Int. J. Rock Mech. Min. Sci.*, *37*(7), 1061–1071, doi:10.1016/S1365-1609(00)00039-3.

Chester, F. M., J. S. Chester, D. L. Kirschner, S. E. Schulz, and J. P. Evans (2004), Structure of large-displacement, strike-slip fault zones in the brittle continental crust, in *Rheology and Deformation of the Lithosphere at Continental Margins*, pp. 223–260, Columbia Univ. Press, New York.

Chester, J. S., F. M. Chester, and A. K. Kronenberg (2005), Fracture surface energy of the Punchbowl fault, San Andreas system, *Nature*, *437*(7055), 133–136, doi:10.1038/nature03942.

Cochard, A., and R. Madariaga (1994), Dynamic faulting under rate-dependent friction, *Pure Appl. Geophys.*, *142*(3–4), 419–445, doi:10.1007/BF00876049.

Colmenares, L. B., and M. D. Zoback (2002), A statistical evaluation of intact rock failure criteria constrained by polyaxial test data for five different rocks, *Int. J. Rock Mech. Min. Sci.*, *39*(6), 695–729.

Dalguer, L. A., K. Irikura, and J. D. Riera (2003a), Generation of new cracks accompanied by the dynamic shear rupture propagation of the 2000 Tottori (Japan) earthquake, *Bull. Seismol. Soc. Am.*, *93*(5), 2236–2252, doi:10.1785/0120020171.

Dalguer, L. A., K. Irikura, and J. D. Riera (2003b), Simulation of tensile crack generation by three-dimensional dynamic shear rupture propagation during an earthquake, *J. Geophys. Res.*, *108*(B3), 2144, doi:10.1029/2001JB001738.

Davis, R. O., and A. P. S. Selvadurai (2002), *Plasticity and Geomechanics*, Cambridge Univ. Press, Cambridge, U. K.

Di Toro, G., R. Han, T. Hirose, N. De Paola, S. Nielsen, K. Mizoguchi, F. Ferri, M. Cocco, and T. Shimamoto (2011), Fault lubrication during earthquakes, *Nature*, *471*, 494–498, doi:10.1038/nature09838.

Dieterich, J. H., and D. E. Smith (2009), Nonplanar faults: Mechanics of slip and off-fault damage, *Pure Appl. Geophys.*, *166*, 1799–1815, doi:10.1007/s00024-009-0517-y.

Drucker, D. C., and W. Prager (1952), Soil mechanics and plastic analysis of limit design, *Q. Appl. Math*, *10*, 157–165.

Duan, B., and S. M. Day (2008), Inelastic strain distribution and seismic radiation from rupture of a fault kink, *J. Geophys. Res.*, *113*, B12311, doi:10.1029/2008JB005847.

Dunham, E. M., D. Belanger, L. Cong, and J. E. Kozdon (2011a), Earthquake ruptures with strongly rate-weakening friction and off-fault plasticity, part 1: Planar faults, *Bull. Seismol. Soc. Am.*, *101*(5), 2296–2307, doi:10.1785/0120100075.

Dunham, E. M., D. Belanger, L. Cong, and J. E. Kozdon (2011b), Earthquake ruptures with strongly rate-weakening friction and off-fault plasticity, part 2: Nonplanar faults, *Bull. Seismol. Soc. Am.*, *101*(5), 2308–2322, doi:10.1785/0120100076.

Esaki, T., S. Du, Y. Mitani, K. Ikusada, and L. Jing (1999), Development of a shear-flow test apparatus and determination of coupled properties for a single rock joint, *Int. J. Rock Mech. Min. Sci.*, *36*(5), 641–650, doi:10.1016/S0148-9062(99)00044-3.

Fang, Z., and E. M. Dunham (2013), Additional shear resistance from fault roughness and stress levels on geometrically complex faults, *J. Geophys. Res.. Solid Earth*, *118*, 3642–3654, doi:10.1002/jgrb.50262.
Faulkner, D. R., T. M. Mitchell, J. Behnsen, T. Hirose, and T. Shimamoto (2011), Stuck in the mud? Earthquake nucleation and propagation through accretionary forearcs, *Geophys. Res. Lett.*, *38*, L18303, doi:10.1029/2011GL048552.
Freund, L. B. (1979), The mechanics of dynamic shear crack propagation, *J. Geophys. Res.*, *84*(8), 2199–2209, doi:10.1029/JB084iB05p02199.
Giacomini, A., O. Buzzi, A. Ferrero, M. Migliazza, and G. Giani (2007), Numerical study of flow anisotropy within a single natural rock joint, *Int. J. Rock Mech. Min. Sci.*, *45*(1), 47–58, doi:10.1016/j.ijrmms.2007.04.007.
Goldsby, D. L., and T. E. Tullis (2011), Flash heating leads to low frictional strength of crustal rocks at earthquake slip rates, *Science*, *334*(6053), 216–218.
Hakami, E. (1995), Aperture distribution of rock apertures, PhD dissertation, Royal Institute of Technology, Stockholm, Sweden.
Harris, R. A., et al. (2009), The SCEC/USGS dynamic earthquake rupture code verification exercise, *Seismol. Res. Lett.*, *80*(1), 119–126, doi:10.1785/gssrl.80.1.119.
Heaton, T. H. (1990), Evidence for and implications of self-healing pulses of slip in earthquake rupture, *Phys. Earth Planet. Inter.*, *64*, 1–20, doi:10.1016/0031-9201(90)90002-F.
Hennings, P., P. Allwardt, P. Paul, C. Zahm, R. Reid, H. Alley, and R. Kirschner (2012), Relationship between fractures, fault zones, stress, and reservoir productivity in the Suban gas field, Sumatra, Indonesia, *AAPG Bull.*, *96*(4), 753–772, doi:10.1306/08161109084.
Hirose, T., and T. Shimamoto (2005), Growth of molten zone as a mechanism of slip weakening of simulated faults in gabbro during frictional melting, *J. Geophys. Res.*, *110*, B05202, doi:10.1029/2004JB003207.
Ida, Y. (1972), Cohesive Force across the Tip of a Longitudinal-Shear Crack and Griffith's Specific Surface Energy, *J. Geophys. Res.*, *77*(20), 3796–3805, doi:10.1029/JB077i020p03796.
Kostrov, B. V. (1964), Self-similar problems of propagation of shear cracks, *J. Appl. Math. Mech.*, *28*, 1077–1087.
Kozdon, J. E., E. M. Dunham, and J. Nordström (2011), Interaction of waves with frictional interfaces using summation-by-parts difference operators: Weak enforcement of nonlinear boundary conditions, *J. Sci. Comput.*, *50*(2), 341–367, doi:10.1007/s10915-011-9485-3.
Kozdon, J. E., E. M. Dunham, and J. Nordström (2012), Simulation of dynamic earthquake ruptures in complex geometries using high-order finite difference methods, *J. Sci. Comput.*, doi:10.1007/s10915-012-9624-5.
Kreiss, H. O., and G. Scherer (1974), in *Mathematical Aspects of Finite Elements in Partial Differential Equations*, edited by C. de Boor, pp. 195–212, New York, Academic Press.
Kreiss, H. O., and G. Scherer (1977), On the existence of energy estimates for difference approximations for hyperbolic systems, Tech. Rep., Dept. of Scientific Computing, Uppsala University, Uppsala, Sweden.
Lee, J. J., and R. L. Bruhn (1996), Structural anisotropy of normal fault surfaces, *J. Struct. Geol.*, *18*(8), 1043–1059, doi:10.1016/0191-8141(96)00022-3.
Lee, H. S., and T. F. Cho (2002), Hydraulic characteristics of rough fractures in linear flow under normal and shear load, *Rock Mech. Rock Eng.*, *35*(4), 299–318, doi:10.1007/s00603-002-0028-y.
Lykotrafitis, G., A. J. Rosakis, and G. Ravichandran (2006), Self-healing pulse-like shear ruptures in the laboratory, *Science*, *313*(5794), 1765–8, doi:10.1126/science.1128359.
Ma, S. (2009), Distinct asymmetry in rupture-induced inelastic strain across dipping faults: An off-fault yielding model, *Geophys. Res. Lett.*, *36*, L20317, doi:10.1029/2009GL040666.
Madariaga, B. Y. R. (1976), Dynamics of expanding circular fault, *Bull. Seismol. Soc. Am.*, *66*(3), 639–666.
Mattsson, K., and J. Nordström (2004), Summation by parts operators for finite difference approximations of second derivatives, *J. Comput. Phys.*, *199*(2), 503–540, doi:10.1016/j.jcp.2004.03.001.
Mitchell, T. M., and D. R. Faulkner (2009), The nature and origin of off-fault damage surrounding strike-slip fault zones with a wide range of displacements: A field study from the Atacama fault system, northern Chile, *J. Struct. Geol.*, *31*(8), 802–816, doi:10.1016/j.jsg.2009.05.002.
Mitchell, T. M., and D. R. Faulkner (2012), Towards quantifying the permeability of fault damage zones in low porosity rocks, *Earth Planet. Sci. Lett.*, *339-340*, 24–31, doi:10.1016/j.epsl.2012.05.014.
Noda, H., E. M. Dunham, and J. R. Rice (2009), Earthquake ruptures with thermal weakening and the operation of major faults at low overall stress levels, *J. Geophys. Res.*, *114*, B07302, doi:10.1029/2008JB006143.
Paul, P., M. D. Zoback, and P. Hennings (2009), Fluid flow in a fractured reservoir using a geomechanically constrained fault-zone-damage model for reservoir simulation, *SPE Reservoir Eval. Eng.*, *12*(4), doi:10.2118/110542-PA.
Power, W. L., and T. E. Tullis (1991), Euclidean and fractal models for the description of rock surface roughness self-similar profile, *J. Geophys. Res.*, *96*(90), 415–424, doi:10.1029/90JB02107.
Power, W. L., and T. E. Tullis (1995), Review of the fractal character of natural fault surfaces with implications for friction and the evolution of fault zones, in *Fractals in the Earth Sciences*, chap. 5, edited by C. C. Barton and P. R. L. Pointe, pp. 89–105, Plenum Press, New York.
Power, L., T. E. Tullis, and J. D. Weeks (1988), Roughness and wear during brittle faulting, *J. Geophys. Res.*, *93*(88), 268–278, doi:10.1029/JB093iB12p15268.
Prakash, V., and F. Yuan (2004), Results of a pilot study to investigate the feasibility of using new experimental techniques to measure sliding resistance at seismic slip rates, AGU Fall Meeting, abstract T21D-02.
Renard, F., C. Voisin, D. Marsan, and J. Schmittbuhl (2006), High resolution 3D laser scanner measurements of a strike-slip fault quantify its morphological anisotropy at all scales, *Geophys. Res. Lett.*, *33*, L04305, doi:10.1029/2005GL025038.
Rice, J. R., C. G. Sammis, and R. Parsons (2005), Off-fault secondary failure induced by a dynamic slip pulse, *Bull. Seismol. Soc. Am.*, *95*(1), 109–134, doi:10.1785/0120030166.
Rudnicki, J. W., and J. R. Rice (1975), Conditions for the localization of deformation in pressure-sensitive dilatant materials, *J. Mech. Phys. Solids*, *23*, 371–394.
Rudnicki, J. W. (1980), Fracture mechanics applied to the Earth's crust, *Annu. Rev. Earth Planet. Sci.*, *8*, 489–525.
Sagy, A., and E. E. Brodsky (2009), Geometric and rheological asperities in an exposed fault zone, *J. Geophys. Res.*, *114*, B02301, doi:10.1029/2008JB005701.
Sagy, A., E. E. Brodsky, and G. J. Axen (2007), Evolution of fault-surface roughness with slip, *Geology*, *35*(3), 283–286, doi:10.1130/G23235A.1.
Savage, H. M., and E. E. Brodsky (2011), Collateral damage: Evolution with displacement of fracture distribution and secondary fault strands in fault damage zones, *J. Geophys. Res.*, *116*, B03405, doi:10.1029/2010JB007665.
Scholz, C. H. (2002), *The Mechanics of Earthquakes and Faulting*, 2nd ed., Cambridge Univ. Press, Cambridge, U. K.
Shipton, Z. K., and P. A. Cowie (2003), A conceptual model for the origin of fault damage zone structures in high-porosity sandstone, *J. Struct. Geol.*, *25*(8), 1343–1345, doi:10.1016/S0191-8141(03)00060-9.

Sleep, N. H. (2010), Application of rate and state friction formalism and flash melting to thin permanent slip zones of major faults, *Geochem. Geophys. Geosyst.*, *11*, Q05007, doi:10.1029/2009GC002997.

Strand, B. (1994), Summation by parts for finite difference approximations for d/dx, *J. Comput. Phys.*, *110*(1), 47–67, doi:10.1006/jcph.1994.1005.

Templeton, E. L., and J. R. Rice (2008), Off-fault plasticity and earthquake rupture dynamics: 1. Dry materials or neglect of fluid pressure changes, *J. Geophys. Res.*, *113*, B09306, doi:10.1029/2007JB005529.

Tsutsumi, A., and T. Shimamoto (1997), High velocity frictional properties of gabbro, *Geophys. Res. Lett.*, *24*(6), 699–702.

Tullis, T. E., and D. L. Goldsby (2003a), Flash melting of crustal rocks at almost seismic slip rates, *Eos Trans. AGU*, *84*(46), Fall Meet. Suppl., Abstract S51B-05.

Tullis, T. E., and D. L. Goldsby (2003b), Laboratory experiments on fault shear resistance relevant to coseismic earthquake slip, SCEC Ann. Prog. Rep., Southern California Earthquake Center.

Viesca, R. C., E. L. Templeton, and J. R. Rice (2008), Off-fault plasticity and earthquake rupture dynamics: 2. Effects of fluid saturation, *J. Geophys. Res.*, *113*, B09307, doi:10.1029/2007JB005530.

Wilson, J., J. Chester, and F. Chester (2003), Microfracture analysis of fault growth and wear processes, Punchbowl Fault, San Andreas system, California, *J. Struct. Geol.*, *25*(11), 1855–1873, doi:10.1016/S0191-8141(03)00036-1.

Yamashita, T. (2000), Generation of microcracks by dynamic shear rupture and its effects on rupture growth and elastic wave radiation, *Geophys. J. Int.*, *143*(2), 395–406, doi:10.1046/j.1365-246X.2000.01238.x.

Yamashita, T. (2009), Rupture dynamics on bimaterial faults and nonlinear off-fault damage, *Int. Geophys.*, 94, 187–215, doi:10.1016/S0074-6142(08)00008-9.

Zheng, G., and J. R. Rice (1998), Conditions under which velocity-weakening friction allows a self-healing versus a cracklike mode of rupture, *Bull. Seismol. Soc. Am.*, *88*(6), 1466–1483.